Power Electronic Systems
Laboratory

Multivariable State Feedback Control of a 500 000 rpm Self-Bearing Motor

T. Baumgartner,
J. W. Kolar

ETH
Eidgenössische Technische Hochschule Zürich
Swiss Federal Institute of Technology Zurich

Multivariable State Feedback Control of a 500 000 rpm Self-Bearing Motor

T. Baumgartner and J.W. Kolar

Power Electronic Systems Laboratory

ETH Zurich

CH-8092 Zurich, Switzerland

baumgartner@lem.ee.ethz.ch

Abstract—**The use of magnetic bearings in electrical drive systems enable very long lifetimes at highest speeds and the operation in high-purity or vacuum environments. The machine prototype presented in this paper overcomes several limitations of previously presented high-speed magnetically-levitated electrical drive systems. Linear bearing characteristics result from the slotless design, which enables applying linear state feedback control without linearization of bearing actuators. A multivariable rotor position control scheme is proposed and its controller performance is analyzed in details. The implemented control scheme proved to perform well in practice, stabilizing the system over the design speed range of the motor with a single set of controller parameters. Measurements of the motor spinning at 500 000 revolutions per minute (rpm) verify the functionality of the overall system. To the authors' knowledge, this is the highest speed achieved by magnetically-levitated electrical drive systems so far.**

I. Introduction

In the last few years, several studies dealing with the design of high-speed electrical drive systems have been published, e.g. [1], [2]. However, the use of today's ultra-high-speed systems in industrial applications has been limited, mainly by the absence of reliable bearings for rotor support and long lifetime of several thousand hours. Promising candidates for high-speed bearings with longer lifetimes are contactless concepts such as active magnetic bearings (AMB) or gas bearings. The focus of this paper is the magnetic bearing, as it is the only contactless bearing technology that can be operated in vacuum or low-pressure environments, such as high-speed optical scanning systems or reaction wheels for attitude control of satellites in orbit.

Most AMB systems built today rely on reluctance force which is generated by guiding a magnetic flux over the air gap between the rotor and the stator. This flux is actively controlled by controlling the bearing winding currents. In the present paper, this bearing topology will be referred to as reluctance-force-based AMB. In contrast, Lorentz-force-based AMB rely on an external magnetic flux density (typically generated by a permanent magnet on the rotor) and electric current densities in bearing windings. The windings are placed in the magnetic air gap of the external flux density. Thus, the bearing force generation is mainly based in Lorentz force in the bearing windings [3], [4].

Several magnetic bearing concepts for rotational speeds beyond 100 000 revolutions per minute (rpm) have been inves-tigated recently. Reluctance-force-based homopolar bearings are presented in [5] and [6]. In [5], a magnetically-levitated milling spindle is presented that achieved a speed of 150 krpm. In [6], a 2 kW machine was operated up to a speed of 120 krpm. In [7], a combined radial-axial reluctance-force-based bearing is presented that was tested up to 120 krpm. However, one of the limitations of achievable actuator bandwidth of reluctance-force-based AMB results from eddy currents in the magnetic circuit's lamination [8]. Furthermore, slot harmonic induced iron losses in the rotor increase with the rotational speed [8], [9]. Due to the poor thermal coupling of the levitated rotor to the rest of the drive system, these losses are crucial. Therefore, a downscaling of a reluctance-force-based AMB system to reach higher rotational speeds is limited amongst others factors by the high rotor losses.

The maximum bearing force of slotless and thus Lorentz-force-based AMB systems is small compared to reluctance-force-based AMB systems [3]. On the other hand, the slotless design of the windings allows to control bearing forces up to high bandwidths [4]. Furthermore, low rotor losses allow for high-speed rotation. Self-bearing motors enable an integration of motor and magnetic bearing what reduces the total length of the rotor when compared to non-integrated AMB systems. The length reduction increases the bending mode frequencies which is beneficial for rotor dynamics of high-speed motors [8]. Similarly to the motor concept proposed in this paper, a slotless and thus Lorentz-force-based high-speed self-bearing motor is presented in [10]. In contrast to the proposed design, a short (slice) rotor was chosen in [10]. Therefore, only two degrees of freedom (DOF) have to be controlled by the magnetic bearing. One DOF is controlled by the motor and three DOF are stabilized passively by reluctance force. The maximum achieved speed of 115 krpm is limited by the mechanical construction of the rotor [10]. A downscaling of the slice motor to reach higher rotational speeds is limited by the passive stabilization of three DOF. The concept of slotless self-bearing motors is applied in [11]–[14] for lower speed applications.

A large variety of methods are proposed in literature for the control of AMB [8]. Generally, a fair and credible comparison of control methods is a very difficult task, as the control performance highly depends on the selection of control parameters. A comparison between centralized and decentralized
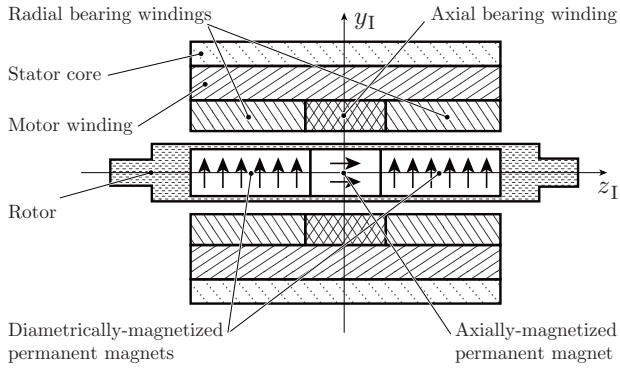
Fig. 1: Simplified machine cross-section through the axis of rotation. The rotor consists of a titanium shaft in which three cylindrical permanent magnets are press fitted. The magnetization direction of the permanent magnets is indicated by the arrows. A slotless amorphous-iron stack is used as stator core. The bearing windings and the motor winding are placed in the magnetic air gap between the rotor and the stator core.

Tab. I: Mechanical properties of the implemented motor prototype.

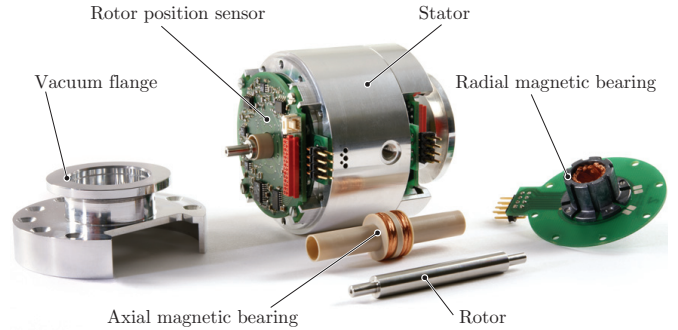| Symbol	Quantity	Value
n_{max}	Maximum rotational speed	500 000 rpm
P_{motor}	Rated motor power	300 W
m	Rotor mass	12.3 g
L_{rotor}	Rotor length	55 mm
D_{rotor}	Rotor diameter	7.3 mm
x_{max}	Maximum rotor deflection	0.25 mm

Fig. 2: Photo of the implemented self-bearing motor with dismantled rotor, axial and radial magnetic bearing.

and also between proportional integral derivative (PID) and linear quadratic (LQ) control methods is presented in [15]. In all cases that were studied in [15], the centralized model-based controllers performed better when compared with the decentralized PID-based solutions.

In many AMB systems built today, particularly in industrial practice, PID regulators are implemented, e.g. [7]. Typically, different regulators are used for different states of the multiple-input multiple-output (MIMO) control problem. Most control algorithms require information of non-measurable system states like radial rotor velocities. Therefore, non-observer based control structures are prone to high-frequency measurement noise that is amplified by the differential part of the controller [16].

The authors of [16] showed that the control performance and the measurement noise rejection of an AMB system can be significantly improved by applying linear quadratic Gaussian (LQG) control algorithm for decentralized magnetic bearing control. In [17], LQ control is presented that is based on a flexible rotor model for an AMB system employing non-linear bearing actuators. In [18], several approaches (including LQR) for the control of a flywheel energy storage device are analyzed. A cross feedback control was selected in [18] due to the strong gyroscopic couplings.

In this paper, the control of a magnetically supported 500 krpm - 300 W motor is presented and measurement results are shown. The focus of this paper is the design of the bearing actuators, the radial rotor position controller and the closed-loop system control performance achieved by the implemented prototype.

The machine prototype is designed for driving optical components such as mirrors in scanning applications. Due to the magnetic bearing, the motor features long lifetime at highest rotational speeds. Furthermore, it can be operated in high-purity or vacuum environments.

II. INTEGRATED BEARING DESIGN

The machine concept of the implemented prototype motor is based on a permanent-magnet synchronous motor (PMSM) proposed in [19]. The magnetic bearing concept is proposed in [3].

A simplified cross-section of the machine is shown in **Fig. 1**. The mechanical data of the prototype is given in **Tab. I** and picture with dismantled magnetic bearing is shown in **Fig. 2**.

As shown in **Fig. 1**, a titanium shaft in which three cylindrical permanent magnets are press fitted is used as rotor of the machine. The magnetic air gap between the rotor and the slotless amorphous-iron stator core is used to place a motor winding and a set of bearing windings. The magnetic field of the two diametrically-magnetized permanent magnets is used for drive torque and radial bearing force generation. The magnetic field of the axially-magnetized permanent magnet is used for the generation of axial bearing force.

Three important effects result from the slotless construction of the windings. Firstly, *linear* and *frequency independent* force/torque-to-winding current relationships result. Secondly, simulations have shown that the rotor eddy-current losses caused by the magnetic field of the bearing windings are negligible. Thirdly, the resulting winding inductances are small compared to slotted designs. Therefore, the bearing currents can be controlled with low reactive power consumption, and low-voltage power electronics using ultra-fast switching frequencies [4]. As a consequence, high bearing actuator bandwidths can be achieved. The listed effects are favorable for ultra-high-speed operation of the machine.
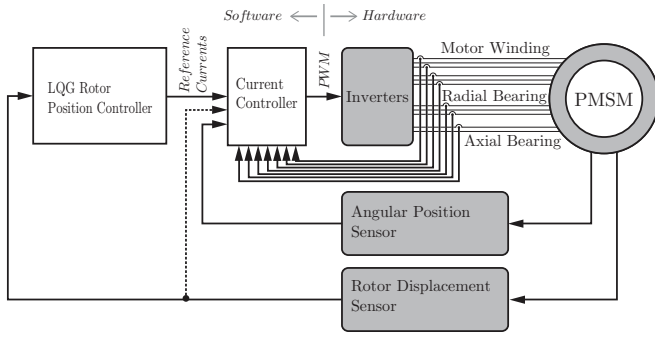
Fig. 3: Control block diagram of the high-speed self-bearing motor [4]. The rotor position is controlled in an outer control loop, whereas the reference winding currents are tracked in an inner control loop.

Fig. 4: Schematic of the rigid rotor geometry and coordinate definitions.

A. Radial Bearing Force Generation

The radial bearing forces are generated in two skewed air-gap windings with a pole-pair number of two. The interested reader is referred to [20] for a detailed description of the used winding type. Due to the heteropolar field of the permanent magnet, the winding currents have to be controlled by a field-oriented control algorithm [3]. According to [4], the radial bearing force vector

$$\boldsymbol{F} = \frac{3}{2}\chi_{\mathrm{pm}} \begin{bmatrix} i_d \\ i_q \\ 0 \end{bmatrix}, \tag{1}$$

can be calculated as a function of field-oriented currents i_d and i_q. The calculation of the bearing constant χ_{pm} is given in [4].

B. Rotor Position Control

The rotor is levitated by controlling the rotor position by means of feedback control. A printed-circuit-board-based position sensor system is implemented for measuring the rotor position in the feedback path of the control scheme. The radial rotor position measurement is based on eddy-current sensors presented in [21], whereas the axial and the angular positions are obtained by Hall-effect-based stray field measurements [4].

A cascaded control scheme shown in **Fig. 3**, as proposed in [4], is used for the control of the rotor position. Radial and axial rotor deflections are measured and controlled in an outer control loop. This controller is implemented in stator-fixed coordinates. The output of the rotor position controller is a set of reference winding currents, which are then tracked in a field-oriented inner control loop. Thus, a measurement of the angular rotor position γ, given by the trigonometric terms $\cos(\gamma)$ and $\sin(\gamma)$, has to be obtained from the angular position sensor.

The implemented bearing power electronics and the control performance of the current control loop are presented in [4].

C. Challenges and Limitations

The biggest challenge for the control of the bearing is the fact that the radial bearing currents have to be controlled by a field-oriente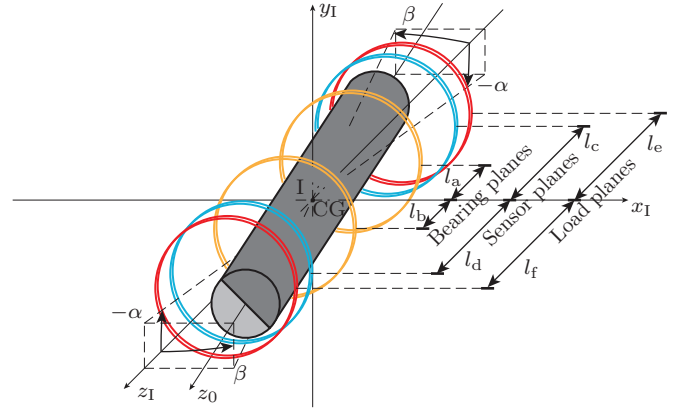d control algorithm up to a rotational frequency of 8.33 kHz. A phase error in the angular transformations results directly in an angular error of the applied radial bearing forces.

Another challenge for the bearing control are the gyroscopic couplings which increase with the rotational speed [8]. Furthermore, the nutation mode frequency increases with the rotational speed [8]. Therefore, high-bandwidth bearing actuators and control are necessary to stabilize the system.

In the proposed design, a bending of the rotor cannot be actively damped. Therefore, the machine has to be operated below the bending mode frequency. Hence, the maximum rotational speed is limited by the mechanical design and dynamics of the rotor.

III. ROTOR DYNAMICS MODELING

This section briefly describes the dynamics of the mechanical system within the AMB control loop. In **Sec. III-A**, the dynamics of a rigid rotor are given. These dynamics are the basis for the design of the rotor position estimator and controller presented in **Sec. IV**. An extended rotor dynamics model accounting for the flexible structure of the rotor is presented in **Sec. III-B**. Both rotor dynamic models will be compared to each other in **Sec. V**.

A. Dynamics of the Rigid Rotor

A schematic of the rotor geometry is shown in **Fig. 4**. A stator-fixed coordinate system I with principal axes $(x_{\mathrm{I}}, y_{\mathrm{I}}, z_{\mathrm{I}})$ and a rotor-fixed coordinate system CG is introduced. The origin of CG is defined as the center of mass of the rotor. The principal axes of CG (x_0, y_0, z_0) coincide with the rotors' principal axes of inertia. The rotor position can be described by the position of CG with respect to I, defined by the transversal displacement $(x_{\mathrm{CG}}, y_{\mathrm{CG}}, z_{\mathrm{CG}})$ and the Cardan angles (α, β, γ).

The definition of radial state dynamics is based on the assumption (i) that the rotor is symmetric and rigid, and (ii) that the deviations of the principal axes of I and CG are small compared to the rotor dimensions. Due to assumption (ii), linearization is applicable, which yields that α and β can be characterized as inclinations about the x_{I}- and y_{I}-axis [8].

349

The equations of motion for the radial state vector

$$\boldsymbol{z} = \begin{bmatrix} \beta & x_{\mathrm{CG}} & -\alpha & y_{\mathrm{CG}} \end{bmatrix}^T, \quad (2)$$

can be derived from Lagranges's equations [8]. For a constant rotational frequency $\Omega = \frac{\partial \gamma}{\partial t}$ and given the assumptions (i) and (ii), the equations of motion can be written in the linearized form [8]

$$M\ddot{\boldsymbol{z}} + G\dot{\boldsymbol{z}} + S\boldsymbol{z} = V\boldsymbol{u} + \boldsymbol{g} + W\boldsymbol{f}_{\mathrm{L}}, \quad (3)$$

where the dot denotes the derivative with respect to time, $\dot{\boldsymbol{z}} = \frac{\partial \boldsymbol{z}}{\partial t}$. The diagonal mass matrix

$$M = \mathrm{diag}\left(I_{y_0}, m, I_{x_0}, m\right), \quad (4)$$

and the gyroscopic coupling matrix

$$G = I_{z_0}\Omega \begin{bmatrix} 0 & 0 & 1 & 0 \\ 0 & 0 & 0 & 0 \\ -1 & 0 & 0 & 0 \\ 0 & 0 & 0 & 0 \end{bmatrix}, \quad (5)$$

are defined according to [8]. m denotes the rotor mass and I_{x_0}, I_{y_0} and I_{z_0} the inertia of the rotor about the x_0-, y_0- and z_0-axis. Given the symmetry of the rotor, $I_{x_0} = I_{y_0}$ can be assumed. The magnetic stiffness, resulting from the high-permeability stator core, is generally a non-linear function of the rotor deflections. It was shown in [3] that for the presented type of machines this force can be approximated by a linear rotor deflection dependent destabilizing force. Therefore, the linear negative stiffness of the configuration is defined by the matrix

$$S = \mathrm{diag}\left(k_\alpha, k_x, k_\alpha, k_x\right). \quad (6)$$

The generalized forces on the right hand side of (3) consist of all external forces acting on the rotor. Such as the force caused by the magnetic bearing current vector

$$\boldsymbol{u} = \begin{bmatrix} i_{d,\mathrm{B1}} & i_{q,\mathrm{B1}} & i_{d,\mathrm{B2}} & i_{q,\mathrm{B2}} \end{bmatrix}^T, \quad (7)$$

the force of gravity caused by the rotor mass

$$\boldsymbol{g} = \begin{bmatrix} T_{y,\mathrm{FF}} & F_{x,\mathrm{FF}} & -T_{x,\mathrm{FF}} & F_{y,\mathrm{FF}} \end{bmatrix}^T, \quad (8)$$

and a force component resulting from an unknown load force

$$\boldsymbol{f}_{\mathrm{L}} = \begin{bmatrix} F_{x,\mathrm{e}} & F_{y,\mathrm{e}} & F_{x,\mathrm{f}} & F_{y,\mathrm{f}} \end{bmatrix}^T. \quad (9)$$

The components of $\boldsymbol{f}_{\mathrm{L}}$ act on the two load planes defined in **Fig. 4**. The transformation of $\boldsymbol{f}_{\mathrm{L}}$ and $\boldsymbol{u}$ into center of mass coordinates is done with the matrices

$$W = \begin{bmatrix} -l_{\mathrm{e}} & 0 & l_{\mathrm{f}} & 0 \\ 1 & 0 & 1 & 0 \\ 0 & -l_{\mathrm{e}} & 0 & l_{\mathrm{f}} \\ 0 & 1 & 0 & 1 \end{bmatrix}, \quad (10)$$
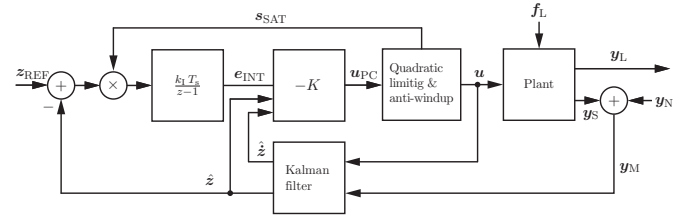

Fig. 5: Proposed multivariable feedback control scheme for the radial rotor position. A LQG controller with integral action and quadratic control input limiting is implemented.

$$V = \frac{3}{2}\chi_{\mathrm{pm}} \begin{bmatrix} -l_{\mathrm{a}} & 0 & l_{\mathrm{b}} & 0 \\ 1 & 0 & 1 & 0 \\ 0 & -l_{\mathrm{a}} & 0 & l_{\mathrm{b}} \\ 0 & 1 & 0 & 1 \end{bmatrix}. \quad (11)$$

Radial displacements of the rotor can be measured at the sensor planes with the embedded eddy-current sensor, yielding the vector $\boldsymbol{y}_{\mathrm{S}}$ or by means of external position sensor at the load planes yielding the vector $\boldsymbol{y}_{\mathrm{L}}$.

B. Dynamics of the Flexible Rotor

The rotor dynamics presented in the previous subsection assume a rigid rotor structure. Thus, possible bending of the rotor is neglected. In order to understand the dynamics including bending effects, a model of the flexible rotor, based on the well-known Euler Bernoulli beam theory [22], is introduced. The model is implemented in state-space representation according to the procedure described [8].

IV. RADIAL ROTOR POSITION CONTROLLER DESIGN

In contrast to most other magnetic bearing concepts, the *linear* and *frequency independent* bearing force-to-current relationship of the proposed design improves the achievable accuracy of system dynamics modeling. Furthermore, the slotless design of the windings allows to control bearing forces up to high bandwidths [4].

The dynamics (3) describe a non-linear, multivariable system. The non-linearity is a result of the gyroscopic effect, which is a function of the time-varying rotational frequency Ω. However, provided that Ω varies only slowly when compared to the radial dynamics, the system behavior is considered as a switched linear system [23]. Thus, for a constant rotational frequency Ω, optimal control algorithms such as $\mathcal{H}_\infty$ or LQG can be applied.

The implemented MIMO linear state feedback control scheme is shown in **Fig. 5**. In order to allow for a computationally efficient and simple real-time implementation of the control algorithm, a LQR and a Kalman filter based on (3), for $\Omega = 0$, is evaluated, i.e. (time-varying) gyroscopic couplings are neglected by the control algorithm. This controller can be implemented very efficiently, in a straight-forward way, using a single set of controller and state estimator matrices over the whole speed range. The closed-loop system performance, including the model error caused by the neglected gyroscopic couplings, is analyzed in **Sec. V**.

A. State Estimation

Since states like radial rotor velocities cannot be measured directly with the employed position sensors, and to allow for position noise rejection, a Kalman filter based on the dynamics (3) is implemented.

The design of the Kalman filter is based on the assumption that the measured rotor position y_S is disturbed by an additive zero-mean white Gaussian noise signal y_N with known covariance matrix. The process noise is defined by the unknown load force vector f_L, which is also assumed to be zero-mean white Gaussian noise with known covariance matrix.

B. Linear State Feedback Controller

A LQR is implemented. In order to allow for offset-free controller performance, the state vector is augmented with an integral of the control error $z_{REF} - \hat{z}$ with respect to time, denoted with e_{INT}. Typically, the reference rotor position is set to the geometric center of the motor, $z_{REF} = 0$.

The calculation of controller matrix K is based on a weighted integral quadratic cost function. The weighting factors for the cost function are chosen such that the required closed-loop system performance is met. The task of controller tuning is therefore reduced to choosing the weights of a single cost function. This results in a significant simplification in practice when compared to PID-based control, where typically different controllers are used for different states of the MIMO system.

C. Quadratic Controller Output Limiting & Anti-Windup

Overheating of the bearing windings can be avoided by limiting the total power loss in the windings. The power loss consists of proximity losses, which are mainly caused by the permanent magnet flux density, and winding current conduction losses, which are proportional to $i_d^2 + i_q^2$ [24]. In the presented prototype, the conduction losses are the dominant loss component. Therefore, only the conduction losses are limited by the controller. Thus, a quadratic limiting function is proposed. The limiting is performed for each of the two bearing windings individually. Both i_d and i_q are scaled with the same factor, preserving the angular direction of the bearing force, but limiting the amplitude of the phase currents to i_{max}. When any of the two bearing windings are in saturation, the integration of the control error $z_{REF} - \hat{z}$ is disabled by the control signal s_{SAT} to prevent integrator windup.

V. RESULTS

The presented control scheme is implemented on an Altera NIOS II signal processor with a controller execution frequency of $33.3\,\text{kHz}$. The achieved controller performance is analyzed in **Sec. V-A**. Finally, measurement results are shown in **Sec. V-B** for a *world record speed* of $500\,\text{krpm}$.

A. Closed-Loop System Performance

A *Campbell diagram* of the closed-loop system is shown in **Fig. 6**. The eigenfrequencies of the closed-loop system are plotted for varying rotational frequency. It can be seen

that the motor was designed such that the bending mode frequencies are higher than the maximum rotational frequency of $500\,\text{krpm}$ ($\Omega = 2\pi \cdot 8.33\,\text{kHz}$). Therefore, it can be assured that the bending resonances are not excited by the unbalance of the rotor [8].

The performance of the controller is analyzed in the frequency domain by the gain of the closed-loop system, shown in **Fig. 5**. The input of the system is defined as force vector f_L, and the output as rotor deflection vector y_L. Single input-to-output transfer functions are a poor performance measurement of a MIMO system, as the gain might vary drastically depending on the direction of the input vector [25]. Therefore, the singular value decomposition is used to analyze the performance of the system. The singular-value input directions of f_L are defined as *forward* and *backward* rotating *parallel* and *conical* disturbances. Similarly, the output directions of y_L are *forward* and *backward* rotating *parallel* and *conical* whirls. Given the symmetry of the motor, it can be seen that the direction of the input is the same as the direction of the output. Therefore, the performance can be analyzed by a set of four singular-value transfer functions.

In **Fig. 7** and **Fig. 8**, singular-value transfer functions are shown using *rigid* and *flexible* rotor model system dynamics. Both models are calculated for the maximum rotational frequency of $500\,\text{krpm}$. In both plots, exactly the same feedback controller is used to stabilize the system. It can be seen that both models yield the same results for all rigid-body modes, which have an eigenfrequency below $1\,\text{kHz}$. In the proposed motor design, all bending modes of the rotor are stable. Therefore, only the rigid-body modes have to be actively controlled by the magnetic bearing. Thus, it can be concluded that it is reasonable to use rigid-body rotor dynamics for the design of the rotor position controller.

In **Fig. 8**, it can be seen that the transfer functions for *conical* disturbances feature peak values at the rigid-body nutation ($575\,\text{Hz}$) and the precession ($81\,\text{Hz}$) frequencies. These peaks are undesirable, but they are unavoidable for real systems [25]. The peak values could be further reduced by including the (time-varying) gyroscopic couplings in the controller design. Nevertheless, it can be concluded from the simulations that the controller yields sufficient performance to stabilize the mechanical system, and it is robust enough to operate the motor over the whole speed range with a single set of controller parameters.

B. Closed-Loop System Measurement at 500 krpm

Fig. 9 shows a measurement of the motor in operation at a rotational speed of $500\,\text{krpm}$. An Ω-synchronous radial rotor deflection of about $\pm 17\,\mu\text{m}$ can be observed. At this rotational speed, Ω is about 14 times higher than the eigenfrequency of the rigid-body modes (**Fig. 6**). Therefore, it can be excluded that the Ω-synchronous deflection is caused by the magnetic bearing. Measurements show that the Ω-synchronous deflections increase with increasing rotational speed. Thus, it can be concluded that the deflections are caused by a deformation of the rotor. This deformation might be caused by unbalance.
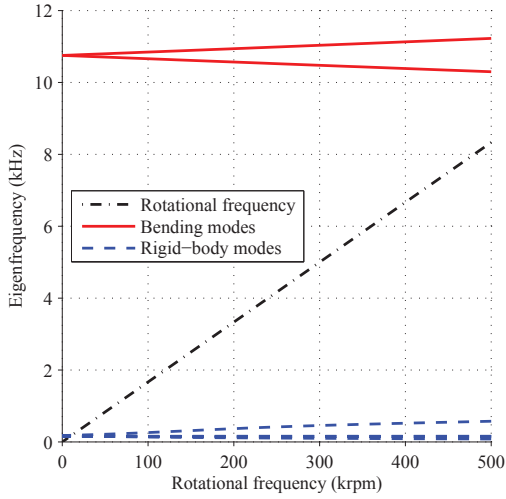
Fig. 6: Campbell diagram for the rated speed range. The eigenfrequencies of the closed-loop system are calculated based on the flexible rotor model system dynamics.
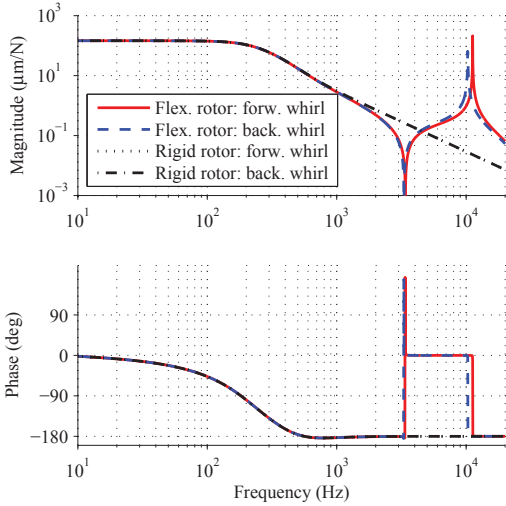

Fig. 7: Calculated closed-loop singular-value transfer functions for forward and backward rotating *parallel* disturbances (f_L) to resulting *parallel* whirls (y_L) for a rotational speed of 500 krpm. Values are given for two systems using the same feedback controller but different rotor dynamics modeling. Both curves using the rigid rotor model (forward and backward whirl) coincide. Therefore, only one curve can be seen in the plot.

Fig. 8: Calculated closed-loop singular-value transfer functions for forward and backward rotating *conical* disturbances (f_L) to resulting *conical* whirls (y_L) for a rotational speed of 500 krpm. Values are given for two systems using the same feedback controller but different rotor dynamics modeling.

Fig. 9: Closed-loop system measurement of the motor in operation at a rotational speed of 500 krpm. The upper plot shows the Hall-effect-based angular position measurement to verify the actual rotational speed. A measurement of the radial rotor deflections obtained by an external optical displacement sensor (Keyence LK-H022) is shown in the center plot. The sensor is positioned to measure radial rotor deflections at the rotor tip. Measured radial bearing phase currents are shown in the lower plot.

VI. CONCLUSION

The machine prototype presented in this paper overcomes several limitations of previously presented high-speed magnetically-levitated electrical drive systems. Both, motor and bearing windings are implemented as air-gap windings. Thus, *linear* and *frequency independent* bearing force-to-current relationships result, improving the accuracy of the system dynamics modeling considerably. Furthermore, the slotless design of the bearing windings allows to achieve very high actuator bandwidths. A multivariable state feedback control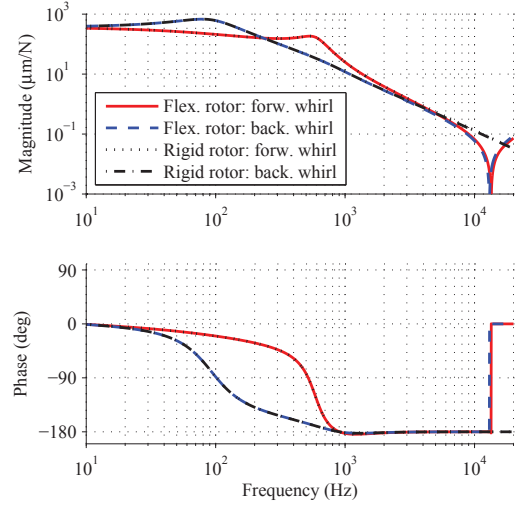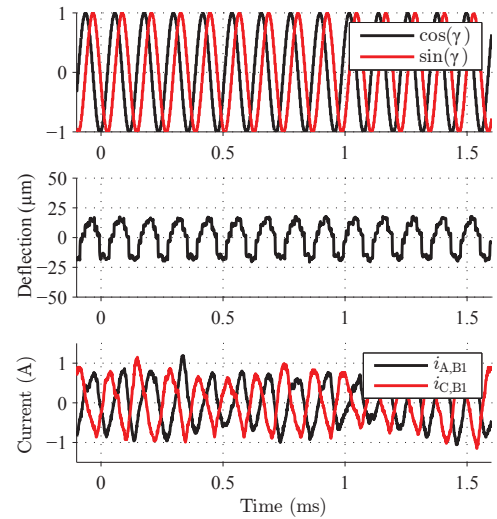 algorithm based on LQG control is proposed. The control scheme is implemented on a signal processor and proved to perform well in practice, stabilizing the system over the design speed range of the high-speed motor with a single set of controller parameters. Closed-loop system measurements of the motor, rotating at 500 000 rpm, verify the functionality of the overall system and prove the feasibility of the proposed control design. To the authors' knowledge, this is the highest speed achieved by magnetically-levitated electrical drive systems so far.

REFERENCES

[1] C. Zwyssig, J. W. Kolar, and S. Round, "Megaspeed drive systems: Pushing beyond 1 million r/min," *IEEE/ASME Transactions on Mechatronics*, vol. 14, no. 5, pp. 564–574, Oct. 2009.

[2] A. Borisavljevic, H. Polinder, and J. Ferreira, "On the speed limits of permanent-magnet machines," *IEEE Transactions on Industrial Electronics*, vol. 57, no. 1, pp. 220–227, Jan. 2010.

[3] T. Baumgartner, A. Looser, C. Zwyssig, and J. W. Kolar, "Novel high-speed, Lorentz-type, slotless self-bearing motor," in *Proceedings of the IEEE Energy Conversion Congress and Exposition (ECCE 2010)*, Sept. 2010, pp. 3971–3977.

[4] T. Baumgartner, R. Burkart, and J. W. Kolar, "Analysis and design of an ultra-high-speed slotless self-bearing permanent-magnet motor," in *Proceedings of the 38th Annual Conference on IEEE Industrial Electronics Society (IECON 2012)*, Oct. 2012, pp. 4459–4465.

[5] M. Kimman, H. Langen, and R. M. Schmidt, "A miniature milling spindle with active magnetic bearings," *Mechatronics*, vol. 20, no. 2, pp. 224–235, 2010.

[6] F. Betschon, "Design principles of integrated magnetic bearings," Ph.D. dissertation, ETH Zurich, Zurich, Switzerland, 2000.

[7] P. Imoberdorf, "Ultrakompakter Antrieb mit radial und axial kombiniertem Magnetlager," Ph.D. dissertation, ETH Zurich, Zurich, Switzerland, 2011.

[8] G. Schweitzer and E. H. Maslen, *Magnetic Bearings*. Berlin Heidelberg: Springer-Verlag, 2009.

[9] H.-Y. Kim and C.-W. Lee, "Analysis of eddy-current loss for design of small active magnetic bearings with solid core and rotor," *IEEE Transactions on Magnetics*, vol. 40, no. 5, pp. 3293–3301, Sept. 2004.

[10] H. Mitterhofer and W. Amrhein, "Design aspects and test results of a high speed bearingless drive," in *Proceedings of the 9th IEEE International Conference on Power Electronics and Drive Systems (PEDS 2011)*, Dec. 2011, pp. 705–710.

[11] Z. Ren and L. Stephens, "Force characteristics and gain determination for a slotless self-bearing motor," *IEEE Transactions on Magnetics*, vol. 42, no. 7, pp. 1849–1860, July 2006.

[12] T. Grochmal and A. Lynch, "Control of a self-bearing servomotor," *IEEE Control Systems*, vol. 29, no. 5, pp. 74–92, Oct. 2009.

[13] H.-I. Lee, S.-Y. Yoo, and M. Noh, "Toroidally-wound self-bearing BLDC motor with Lorentz force," *IEEE Transactions on Magnetics*, vol. 46, no. 6, pp. 2148–2151, June 2010.

[14] S. Ueno and T. Kato, "A novel design of a Lorentz-force-type small self-bearing motor," in *Proceedings of the IEEE International Conference on Power Electronics and Drive Systems (PEDS 2009)*, Nov. 2009, pp. 926–931.

[15] R. P. Jastrzebski and R. Pllnen, "Centralized optimal position control for active magnetic bearings: comparison with decentralized control," *Electrical Engineering*, vol. 91, pp. 101–114, 2009.

[16] T. Schuhmann, W. Hofmann, and R. Werner, "Improving operational performance of active magnetic bearings using Kalman filter and state feedback control," *IEEE Transactions on Industrial Electronics*, vol. 59, no. 2, pp. 821–829, Feb. 2012.

[17] R. P. Jastrzebski, "Design and implementation of FPGA-based LQ control of active magnetic bearings," Ph.D. dissertation, Lappeenranta University of Technology, Lappeenranta, Finland, 2007.

[18] M. Ahrens, L. Kucera, and R. Larsonneur, "Performance of a magnetically suspended flywheel energy storage device," *IEEE Transactions on Control Systems Technology*, vol. 4, no. 5, pp. 494–502, Sep. 1996.

[19] C. Zwyssig, S. Round, and J. W. Kolar, "An ultrahigh-speed, low power electrical drive system," *IEEE Transactions on Industrial Electronics*, vol. 55, no. 2, pp. 577–585, Feb. 2008.

[20] A. Looser, T. Baumgartner, J. W. Kolar, and C. Zwyssig, "Analysis and measurement of three-dimensional torque and forces for slotless permanent-magnet motors," *IEEE Transactions on Industry Applications*, vol. 48, no. 4, pp. 1258–1266, July–Aug. 2012.

[21] A. Muesing, C. Zingerli, P. Imoberdorf, and J. W. Kolar, "PEEC-based numerical optimization of compact radial position sensors for active magnetic bearings," in *Proceedings of the 5th IEEE International Conference on Integrated Power Systems (CIPS 2008)*, March 2008, pp. 1–5.

[22] R. Craig and A. Kurdila, *Fundamentals of Structural Dynamics*. Wiley, 2011.

[23] H. Khalil, *Nonlinear Systems*. Prentice Hall, 2002.

[24] C. Zwyssig, "An ultra-high-speed electrical drive system," Ph.D. dissertation, ETH Zurich, Zurich, Switzerland, 2008.

[25] S. Skogestad and I. Postlethwaite, *Multivariable feedback control: analysis and design*, 2nd ed. Wiley, 2005.